

# Mesoscale multi-physics simulation of rapid solidification of Ti-6Al-4V alloy

Dehao Liu, Yan Wang\*

*Woodruff School of Mechanical Engineering, Georgia Institute of Technology, Atlanta, GA 30332, USA*

\*Corresponding author. Tel.: +1 404-894-4714; fax: +1 404-894-9342.

E-mail address: yan.wang@me.gatech.edu (Yan Wang).

## **Abstract**

Powder bed fusion is a recently developed additive manufacturing (AM) technique for alloys, which builds parts by selectively melting metallic powders with a high-energy laser or electron beam. Nevertheless, there is still a lack of fundamental understanding of the rapid solidification process for better quality control. To simulate the microstructure evolution of alloys during the rapid solidification, in this research, a mesoscale multi-physics model is developed to simultaneously consider solute transport, phase transition, heat transfer, latent heat, and melt flow. In this model, the phase-field method simulates the dendrite growth of alloys, whereas the thermal lattice Boltzmann method models heat transfer and fluid flow. The phase-field method and the thermal lattice Boltzmann method are tightly coupled. The simulation results of Ti-6Al-4V show that the consideration of latent heat is necessary because it reveals the details of the formation of secondary arms and provides more realistic kinetics of dendrite growth. The proposed multi-physics simulation model provides new insights into the complex solidification process in AM.

*Keywords:* selective laser melting; Ti-6Al-4V; dendrite growth; phase-field method; thermal lattice Boltzmann method

## 1. Introduction

Understanding solidification is critical to control the quality of parts built with metallic additive manufacturing (AM) processes, which include selective laser melting (SLM), electron beam melting (EBM), direct energy deposition (DED), and others. Different alloys have been used in metal-based AM processes. Particularly, titanium alloy Ti-6Al-4V has a wide range of applications from aerospace to biomedical devices. As a high strength ( $\alpha + \beta$ ) titanium alloy, Ti-6Al-4V's microstructure mainly depends on its chemical composition, processing condition, and heat treatment history. During the complex process of solidification, interactions between solute diffusion, heat transfer, and fluid dynamics have significant effects on the formation of the final solid microstructure. Fundamental understanding of the process allows us to predict the solidified microstructure and the physical properties of the solids for process design and optimization. To understand the solidification of Ti-6Al-4V, simulations at the mesoscale are cost-effective alternatives to expensive experiments for in-situ observation.

Compared to atomistic scale simulations, mesoscale models such as phase-field method (PFM) [1–7] and cellular automaton (CA) simulate solidification more efficiently. PFM simulates a much longer time scale than what molecular dynamics is able to, and provides more physical details of material phases than what Monte Carlo simulation can. Although PFM is computationally more expensive than CA, it provides fine-grained details. It has been shown that the steady state dendrite tip velocities predicted by PFM agree with the Lipton-Glicksman-Kurz model more closely than CA results do [8].

To distinguish between liquid and solid phases, a continuous variable, namely *order parameter* or *phase field*  $\phi$ , is used in PFM. The evolution of the microstructure in solidification is modeled by partial differential equations of the phase field  $\phi$ . PFM has been used to simulate complex phase transitions of multicomponent multiphase alloys [9–14].

Recently PFM was adopted to simulate the grain growth of Ti-6Al-4V alloy in the EBM process [15,16]. It has been revealed that increases in temperature gradient and beam scanning speed reduce the primary arm spacing of columnar dendrites. However, the above work did not account for the effects of melt flow and latent heat, which are critical for the formation of the solid microstructure.

Compared to traditional finite volume methods to simulate fluid flow, the lattice Boltzmann method (LBM) has computational advantages for systems with complex boundaries [17–19]. LBM is capable of simulating single-phase and multiphase flow with complex boundary conditions and multiphase interfaces. To incorporate thermal effects into fluid dynamics, the thermal lattice Boltzmann method (TLBM) [20–26] has been developed. Unlike LBM, which uses a single particle distribution function for fluids, TLBM uses two distinct particle distribution functions for fluid dynamics and heat transfer. TLBM has been recently adopted to simulate the evolution of temperature and velocity fields in the EBM process [27]. However, the simulation using TLBM alone lacks fine-grained phase information, because it cannot simulate the evolution of dendrite structure.

Some efforts have been made to combine PFM and LBM to simulate the dendritic growth in solidification of pure metals and alloys [28–32], allowing for interplay between grain growth and melt flow. A combination of three-dimensional (3D) PFM and LBM has been adopted to simulate the grain growth of Al-Cu alloy in a melt flow [33]. However, in these PFM and LBM combinations, either the isothermal condition or a one-dimensional temperature field was assumed [34], which oversimplifies the physical processes. The temperature field during rapid solidification can be much more complex than that of solidification under the equilibrium thermal condition because melt flow and the release of latent heat will constantly change the temperature distribution. Therefore, the effects of latent heat and fluid flow on phase transition should be simultaneously considered in the multi-physics modeling of solidification for accurate prediction.

Here, a new integrated phase-field and thermal lattice Boltzmann method (PF-TLBM) is proposed to simulate rapid solidification of Ti-6Al-4V alloy by concurrently coupling solute transport, heat transfer, latent heat, and fluid dynamics. In the most similar work by Sakane et al. [33], PF and LBM were combined without considering heat transfer. To the best of our knowledge, this is the first time that PF and TLBM have been combined to predict the complex process of rapid solidification, with multi-physics considerations of phase transition, fluid dynamics, heat transfer, and latent heat effects. The simulation results show that the consideration of latent heat is important because it reveals the details of the formation of secondary arms and provides more realistic kinetics of dendrite growth. In addition, the effect of melt flow is subdued by high cooling rate because dendrites grow very quickly in rapid solidification.

In the remainder of this paper, the formulation of the proposed PF-TLBM model is described in Section 2. The simulation results and effects of latent heat and melt flow on the dendrite growth are shown in Section 3, which also contains experimental comparison, sensitivity analysis of mesh sizes, as well as quantitative analyses of the temperature gradient, growth velocity, and their combinations.

## **2. Methodology**

In the PF-TLBM model, phase formation is described with partial differential equations of phase field and composition variables, whereas fluid flow and thermal effects are modeled with convection-diffusion equations of velocity and temperature fields, respectively. Information exchange between the phase, temperature, and velocity fields are achieved by

updating the variables in each iteration of simulation. The latent heat effect is also incorporated in the simulation of heat transfer. The PF-TLBM model proposed here is an extension of our recent work [35]. In the extension, a local non-equilibrium partition coefficient is considered for rapid solidification, and a variable grid computational scheme is developed to simulate the phase field and the temperature field. A coarser grid is used in TLBM to improve simulation efficiency and accuracy because the thermal diffusivity and solute diffusivity differ by three orders of magnitude.

## 2.1 Phase-field method

The multi-phase multi-component phase-field method is a generic formulation for phase transitions of alloys. In this work, the multi-phase field method described in Ref. [30] is adopted. The essential component of PFM is a free energy functional that describes the kinetics of phase transition. The free energy functional

$$F = \int_{\Omega} (f^{GB} + f^{CH}) dV \quad (1)$$

is defined with an interfacial free energy density  $f^{GB}$  and a chemical free energy density  $f^{CH}$  in a domain  $\Omega$ .

A continuous variable called phased field,  $\phi$ , indicates the fraction of the solid phase in the simulation domain during the solidification process, and the fraction of the liquid phase is  $\phi_l = 1 - \phi$ . The interfacial free energy density is defined as

$$f^{GB} = \frac{4\sigma^*(\mathbf{n})}{\eta} \left\{ |\nabla\phi|^2 + \frac{\pi^2}{\eta^2} \phi(1-\phi) \right\}, \quad (2)$$

where  $\sigma^*(\mathbf{n})$  is the anisotropic interfacial energy stiffness,  $\eta$  is the interfacial width, and  $\mathbf{n} = \nabla\phi / |\nabla\phi|$  is the local normal direction of the interface. The anisotropic interfacial energy stiffness is defined as

$$\sigma^* = \sigma + \frac{\partial^2 \sigma}{\partial \theta^2} = \sigma_0^* \left[ 1 - 3\varepsilon^* + 4\varepsilon^* (n_x^4 + n_y^4) \right] \quad (3)$$

where  $\sigma$  is the interfacial energy,  $\theta = \arctan(n_y / n_x)$  indicates the orientation,  $\sigma_0^*$  is the prefactor of interfacial energy stiffness, and  $\varepsilon^*$  is the anisotropy strength of interfacial energy stiffness, which models the difference between the primary and secondary growth directions of dendrites.

The chemical free energy is the combination of bulk free energies of individual phases

$$f^{CH} = h(\phi) f_s(C_s) + h(1-\phi) f_l(C_l) + \mu \left[ C - (\phi C_s + \phi_l C_l) \right], \quad (4)$$

where  $C_s$  and  $C_l$  are the weight percentages (wt%) of solute in the solid or liquid phase, respectively.  $C$  is the overall composition of a solution in the simulation domain.  $f_s(C_s)$  and  $f_l(C_l)$  are the chemical bulk free energy densities of solid and liquid phases, respectively.

$\mu$  is the generalized chemical potential of solute introduced as a Lagrange multiplier to conserve the solute mass balance  $C = \phi C_s + \phi_l C_l$ . The weight function

$$h(\phi) = \frac{1}{4} [(2\phi - 1) \sqrt{\phi(1-\phi)} + \frac{1}{2} \arcsin(2\phi - 1)] \quad (5)$$

provides the coefficients associated with solid and liquid bulk energies.

The evolution of the phase field is described by

$$\dot{\phi} = M_\phi \left\{ \sigma^*(\mathbf{n}) \left[ \nabla^2 \phi + \frac{\pi^2}{\eta^2} \left( \phi - \frac{1}{2} \right) \right] + \frac{\pi}{\eta} \sqrt{\phi(1-\phi)} \Delta G \right\}, \quad (6)$$

where  $M_\phi$  is the coefficient of interface mobility, and the driving force is given by

$$\Delta G = \Delta S (T_m - T - m_l C_l), \quad (7)$$

where  $\Delta S = -1 \times 10^6 \text{ J} \cdot \text{K}^{-1}$  is the entropy difference between solid and liquid phases,  $T_m$  is the melting temperature of a pure substance,  $T$  is the temperature field, and  $m_l$  is the slope of liquidus. Existing studies of interface mobility are restricted to pure metal or one-component systems. For the complex ternary alloy Ti-6Al-4V, there is a lack of information to reveal the dependency of interface mobility on temperature. For simplification, the interface mobility is

assumed to be constant in this work.

The evolution of the composition is modeled by

$$\dot{C} + \mathbf{u}_l \cdot \nabla [(1-\phi)C_l] = \nabla \cdot [D_l(1-\phi)\nabla C_l] + \nabla \cdot \mathbf{j}_{at}, \quad (8)$$

where  $\mathbf{u}_l$  is the velocity of the liquid phase, and  $k = C_s / C_l$  is the local partition coefficient.

During rapid solidification, the assumption of local composition equilibrium is not reasonable. Therefore, the local non-equilibrium partition coefficient  $k$  is computed based on Aziz's model [36,37]

$$k = \frac{k_e + V\lambda / D_l}{1 + V\lambda / D_l}, \quad (9)$$

where  $k_e = 0.206$  is the equilibrium partition coefficient,  $\lambda = 3 \times 10^{-9}$  m is the actual interface width in atomic dimensions, and  $V = \dot{\phi} / |\nabla \phi|$  is the local velocity of the interface.

$D_l$  is the diffusion coefficient of liquid, which is assumed to follow an Arrhenius form with an activation energy of 250 kJ·mol<sup>-1</sup> based on [38]

$$D_l = 10^{-8} \times \exp\left(\frac{250000}{RT_l} - \frac{250000}{RT}\right), \quad (10)$$

where  $T_l$  is the liquidus temperature and  $R$  is gas constant. Furthermore,  $\mathbf{j}_{at}$  is the anti-trapping current and defined as

$$\mathbf{j}_{at} = \frac{\eta}{\pi} \sqrt{\phi(1-\phi)} (C_l - C_s) \dot{\phi} \frac{\nabla \phi}{|\nabla \phi|}, \quad (11)$$

which is used to eliminate the unphysical solute trapping during the interface diffusion process. It removes the anomalous chemical potential jump [6,39] so that simulations can be done more efficiently with the simulated interface width exceeding that of the physical one.

Eqs.(6) and (8) are the main equations to solve during the phase field simulation. The anti-trapping current was originally introduced for the quasi-equilibrium condition. For

simplification, it is still used here under the non-equilibrium condition for rapid solidification, since here the simulated domain size 90  $\mu\text{m}$  is small and the simulated time period 1.4 ms is short. The upwind scheme of the finite difference method is applied to solve Eqs.(6) and (8).

## 2.2 Thermal lattice Boltzmann method

The conservation equations of mass, momentum, and energy are given by

$$\nabla \cdot (\phi_l \mathbf{u}_l) = 0, \quad (12)$$

$$\frac{\partial}{\partial t} (\phi_l \mathbf{u}_l) + \nabla \cdot (\phi_l \mathbf{u}_l \mathbf{u}_l) = -\frac{\phi_l}{\rho} \nabla P + \nabla \cdot [\nu \nabla (\phi_l \mathbf{u}_l)] + \mathbf{F}_d, \quad (13)$$

$$\frac{\partial T}{\partial t} + \nabla \cdot (\phi_l \mathbf{u}_l T) = \nabla \cdot (\alpha \nabla T) + q, \quad (14)$$

respectively, where  $\mathbf{u}_l$  is the velocity of liquid with density  $\rho$ ,  $P$  is the pressure,  $\nu$  is the coefficient of kinematic viscosity,  $\alpha$  is the thermal diffusivity, and

$$\mathbf{F}_d = -h^* (1 - \phi) \rho \nu \frac{\phi^2}{\eta^2} \mathbf{u}_l \quad (15)$$

is the dissipative force caused by the interaction between solid and liquid phases, where  $h^* = 147$  is a coefficient fitted from the calculation of Poiseuille flow in a channel with diffuse walls [30]. Furthermore,

$$q = \frac{L_H}{c_p} \frac{\partial \phi}{\partial t} \quad (16)$$

is the released latent heat during solidification, where  $L_H$  is the latent heat of fusion, and  $c_p$  is the specific heat capacity.

Instead of solving Eqs.(12)-(14) directly, particle distribution functions for density  $f_i(\mathbf{x}, t)$  and temperature  $g_i(\mathbf{x}, t)$  are used to capture the dynamics of the system in TLBM. The macroscopic properties of velocity  $\mathbf{u}_l$  and temperature  $T$  can be calculated based on the density and temperature distribution functions. In the TLBM model, the spatial domain is discretized as a lattice. Particles move dynamically between neighboring lattice nodes. In a two-dimensional D2Q9 model, each node has eight neighbors. The velocity vector

$$\mathbf{e}_i = \begin{cases} (0, 0), & i = 0 \\ (\pm c, 0), (0, \pm c), & i = 1, \dots, 4 \\ (\pm c, \pm c), & i = 5, \dots, 8 \end{cases} \quad (17)$$

represents the velocity along the  $i$ -th direction in the lattice with respect to a reference node, where  $c = \Delta x / \Delta t$  is the lattice velocity with spatial resolution  $\Delta x$  and time step  $\Delta t$ ,  $i=0$  is the reference lattice node, and  $i=1$  to 4 indicate the right, top, left, and down directions, whereas  $i=5$  to 8 indicate the top-right, top-left, down-left, and down-right directions, respectively.

The evolution of particle distribution for density  $f_i$  is modeled by

$$f_i(\mathbf{x} + \mathbf{e}_i \Delta t, t + \Delta t) - f_i(\mathbf{x}, t) = \frac{1}{\tau_f} [f_i^{eq}(\mathbf{x}, t) - f_i(\mathbf{x}, t)] + F_i(\mathbf{x}, t) \quad (18)$$

where

$$\tau_f = \frac{\nu}{c_s^2 \Delta t} + 0.5 \quad (19)$$

is a dimensionless relaxation time parameter with the speed of sound  $c_s^2 = c^2 / 3$ ,

$$f_i^{eq}(\mathbf{x}, t) = \omega_i \rho \left[ 1 + \frac{\mathbf{e}_i \cdot \mathbf{u}_l}{c_s^2} + \frac{(\mathbf{e}_i \cdot \mathbf{u}_l)^2}{2c_s^4} - \frac{\mathbf{u}_l^2}{2c_s^2} \right] \quad (20)$$

is the equilibrium distribution, and

$$F_i = \left( 1 - \frac{1}{2\tau_f} \right) \omega_i \left( \frac{\mathbf{e}_i - \mathbf{u}_l}{c_s^2} + \frac{\mathbf{e}_i \cdot \mathbf{u}_l}{c_s^4} \mathbf{e}_i \right) \cdot \mathbf{F}_d \quad (21)$$

is the force source [25,40], where  $\omega_i$  represents the weight associated with direction  $i$ . In

the two-dimensional D2Q9 model, they are

$$\omega_i = \begin{cases} 4/9, & i = 0 \\ 1/9, & i = 1, \dots, 4 \\ 1/36, & i = 5, \dots, 8 \end{cases} \quad (22)$$

The evolution of particle distribution for temperature  $g_i$  is modeled in parallel by

$$g_i(\mathbf{x} + \mathbf{e}_i \Delta t, t + \Delta t) - g_i(\mathbf{x}, t) = \frac{1}{\tau_g} [g_i^{eq}(\mathbf{x}, t) - g_i(\mathbf{x}, t)] + Q_i(\mathbf{x}, t) \quad (23)$$

where

$$\tau_g = \frac{\alpha}{c_s^2 \Delta t} + 0.5 \quad (24)$$

is similarly a dimensionless relaxation time parameter,

$$g_i^{eq}(\mathbf{x}, t) = \omega_i T \left[ 1 + \frac{\mathbf{e}_i \cdot \mathbf{u}_l}{c_s^2} + \frac{(\mathbf{e}_i \cdot \mathbf{u}_l)^2}{2c_s^4} - \frac{\mathbf{u}_l^2}{2c_s^2} \right] \quad (25)$$

is the equilibrium distribution, and

$$Q_i = \left( 1 - \frac{1}{2\tau_g} \right) \omega_i q \quad (26)$$

is the heat source.

Eqs.(18) and (23) are the main equations to be solved in TLBM, based on which density and temperature distributions are updated at each time step. During a simulation, the macroscopic quantities of density, velocity, and temperature can be calculated from  $f_i$ 's and  $g_i$ 's as

$$\rho = \sum_i f_i, \quad (27)$$

$$\rho \mathbf{u}_l = \sum_i \mathbf{e}_i f_i + \frac{\Delta t}{2} \mathbf{F}_i, \quad (28)$$

$$T = \sum_i g_i + \frac{\Delta t}{2} Q_i, \quad (29)$$

respectively. At each iteration, the properties are calculated, and Eqs.(18) and (23) are updated accordingly.

In rapid solidification, heat transfer is much faster than solute diffusion, where thermal diffusivity can be three orders of magnitude larger than solute diffusivity. In this work, to reduce the computational cost and improve accuracy, a fine grid spacing  $dx$  is used for the PFM simulation, whereas a coarse grid spacing  $\Delta x = 30 dx$  is used for the TLBM simulation. The same time step  $\Delta t$  is used for both simulations. The results of PFM are averaged and

transferred to the TLBM model, while the results of TLBM are linearly interpolated as the input for the PFM model. To satisfy the no-slip boundary condition, a bounce-back scheme is used at the solid-liquid interface. The density distribution function at the boundary node  $f_{\bar{i}}(\mathbf{x}_b, t + \Delta t)$  with the direction  $\bar{i}$  such that  $\mathbf{e}_{\bar{i}} = -\mathbf{e}_i$  is determined by

$$f_{\bar{i}}(\mathbf{x}_b, t + \Delta t) = f_i(\mathbf{x}_b, t) + \frac{1}{\tau_f} [f_i^{eq}(\mathbf{x}_b, t) - f_i(\mathbf{x}_b, t)] - 6\omega_i \rho_w \frac{\mathbf{e}_i \cdot \mathbf{u}_w}{c^2} \quad (30)$$

where  $\mathbf{u}_w$  is the velocity of the moving wall at the location  $\mathbf{x}_w = \mathbf{x}_b + \frac{1}{2}\mathbf{e}_i\Delta t$  and  $\rho_w$  is the density at the wall. For the thermal boundary condition, an anti-bounceback scheme [41–43] is used. At the boundary, the temperature distribution function  $g_{\bar{i}}(\mathbf{x}_b, t + \Delta t)$  is given by

$$g_{\bar{i}}(\mathbf{x}_b, t + \Delta t) = -g_i(\mathbf{x}, t) - \frac{1}{\tau_g} [g_i^{eq}(\mathbf{x}, t) - g_i(\mathbf{x}, t)] + 2\omega_i T_w \left[ 1.0 + 4.5 \frac{(\mathbf{e}_i \cdot \mathbf{u}_w)^2}{c^2} - 1.5 \frac{|\mathbf{u}_w|^2}{c^2} \right] \quad (31)$$

where

$$T_w = T_b - \frac{q_H \Delta x}{2\kappa} \quad (32)$$

is the temperature of the wall calculated based on the outward heat flux  $q_H$  at the boundary and the thermal conductivity of the material  $\kappa$ .

### 2.3 PF-TLBM algorithm implementation

In the multi-physics PF-TLBM simulation, different variables are tightly coupled, including liquid velocity  $\mathbf{u}_l$ , composition  $C$ , temperature  $T$ , and phase field  $\phi$  and its time derivative  $\dot{\phi}$ . Fig. 1 illustrates the algorithm of PF-TLBM. The composition is first calculated based on the initial temperature and phase field by solving Eq. (8) with the finite difference method. Then phase field is updated based on Eq. (6) with the updated composition values. The dissipative force in Eq. (15) is updated with the latest values of the phase field. The total force applied in LBM as in Eq. (21) is then updated. Temperature and liquid velocity field are coupled in TLBM as in Eq. (25). The updated velocity values are passed to update the

composition by solving the advection equations. The updated temperature and fluid velocity in TLBM are then used in PFM for the next iteration. The proposed PF-TLBM algorithm is implemented and integrated with the open-source phase field simulation toolkit OpenPhase [44].

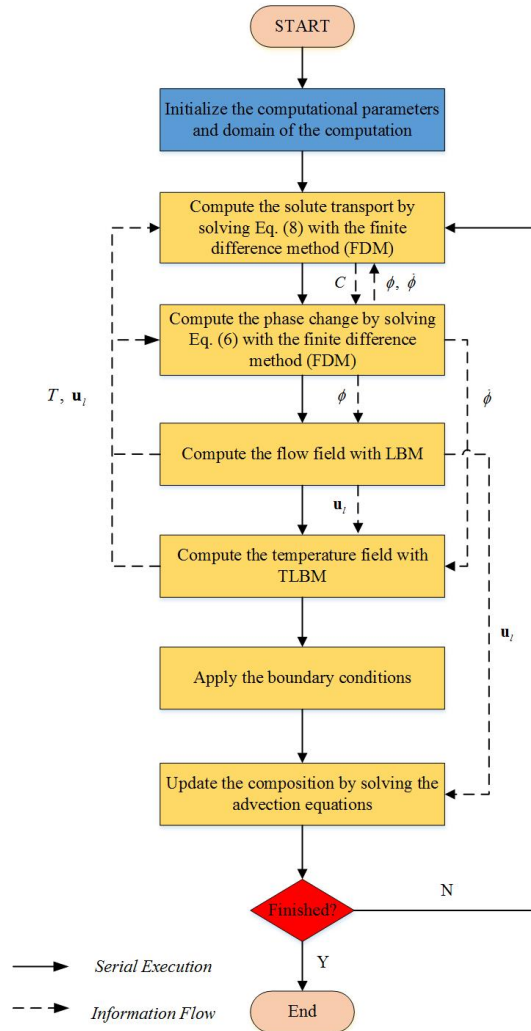


Fig. 1. The flow chart of the PF-TLBM simulation algorithm

### 3. Simulation results and discussion

Here, Ti-6Al-4V alloy is used to demonstrate the PF-TLBM simulation scheme. In this model, the ternary Ti-6Al-4V alloy is treated as a binary alloy, and the solute is the combination of Al and V. This pseudo-binary approach is similar to the existing work [15,45], which was shown to be an effective replacement of the multi-component approach for modeling solidification kinetics of Ti-6Al-4V alloy. The physical properties of Ti-6Al-4V alloy are given in Table 1 [30].

In order to reduce or eliminate the effect of numerical solute trapping, the fine grid spacing  $dx$  should be smaller than the solute diffusion length  $D_l/V$ , where  $D_l$  is solute diffusivity and  $V$  is interface velocity. The maximum dendrite growth velocity is assumed to be  $V_{\max} = 50$  mm/s. Therefore, a fine grid spacing  $dx = 0.1 \mu\text{m}$  and a coarse grid spacing  $\Delta x = 30 dx = 3 \mu\text{m}$  are adopted. Based on the von Neumann stability analysis or Fourier stability analysis, the upper limit of the time step is  $\Delta t \leq \min\{dx^2/4D_l, \Delta x^2/4\nu, \Delta x^2/4\alpha\}$ . Therefore, the time step  $\Delta t = 0.1 \mu\text{s}$  is applied in all simulation runs. The initial temperature is  $T = 1920$  K, which means that the undercooling is 8 K given the initial composition. The length of the simulated domain is  $L_x = 900 dx$  in the  $x$ -direction and the width is  $L_y = 900 dx$  in the  $y$ -direction. The initial radius of the nucleus is  $D = 9 dx$  and the interface width is  $\eta = 5 dx$ , which means that there are 6 nodes on the interface or boundary layer. The initial composition of the solute is set as  $C_0 = 10$  wt% for the whole simulation domain. The setup of boundary conditions for all simulations is schematically illustrated in Fig. 2. Zero Neumann conditions are set at the bottom  $y = 0$  and top  $y = L_y$  boundaries for the phase field  $\phi$  and composition  $C$ . Although the change of temperature gradient within the melt pool will affect the grain structure and grain size distribution [46], the change of temperature gradient can be assumed to be small given the fact that the small simulation domain is small compared with the whole melt pool. A fixed heat flux  $q_H = \rho c_p L_y \dot{T}$  [10] is set at the bottom boundary given the constant cooling rate  $\dot{T} = 5 \times 10^4$  K/s, while an adiabatic boundary condition is set at the top boundary. When the dendrite grows in a forced flow, a constant flow velocity  $|\mathbf{u}_w| = 0.1$  m/s is imposed at the top boundary of the domain. Periodic boundary conditions are set at the left  $x = 0$  and right  $x = L_x$  boundaries for the phase field  $\phi$ , composition  $C$ , temperature  $T$ , and flow  $\mathbf{u}_l$ . The nuclei are located at the bottom cold wall with constant heat flux to simulate the directional dendrite growth in selective laser melting. The locations of the three nuclei are  $x = 10 \mu\text{m}$ ,  $45 \mu\text{m}$ , and  $80 \mu\text{m}$ , respectively. To compare the simulation

results with the experiments done by Simonelli et al. [47], the orientation of the three nuclei is set to be almost the same as the orientation of reconstructed  $\beta$  grains based on the electron backscatter diffraction (EBSD) data.

Table 1. Physical properties of Ti-6Al-4V alloy

Physical properties	Value
Melting point of pure Ti, $T_m$ [K]	1941
Liquidus temperature, $T_l$ [K]	1928
Solidus temperature, $T_s$ [K]	1878
Liquidus slope, $m_l$ [K/wt%]	-1.3
Equilibrium partition coefficient, $k_e$	0.206
Prefactor of interfacial energy stiffness, $\sigma_0^*$ [J/m <sup>2</sup> ]	0.5
Interfacial energy stiffness anisotropy, $\varepsilon^*$	0.35
Interface mobility, $M_\phi$ [m <sup>4</sup> /(J · s)]	$1.2 \times 10^{-8}$
Kinematic viscosity, $\nu$ [m <sup>2</sup> /s]	$6.11 \times 10^{-7}$
Thermal diffusivity, $\alpha$ [m <sup>2</sup> /s]	$8.1 \times 10^{-6}$
Latent heat of fusion, $L_H$ [J/kg]	$2.90 \times 10^5$
Specific heat capacity, $c_p$ [J/(kg · K)]	872
Density, $\rho$ [kg/m <sup>3</sup> ]	4000

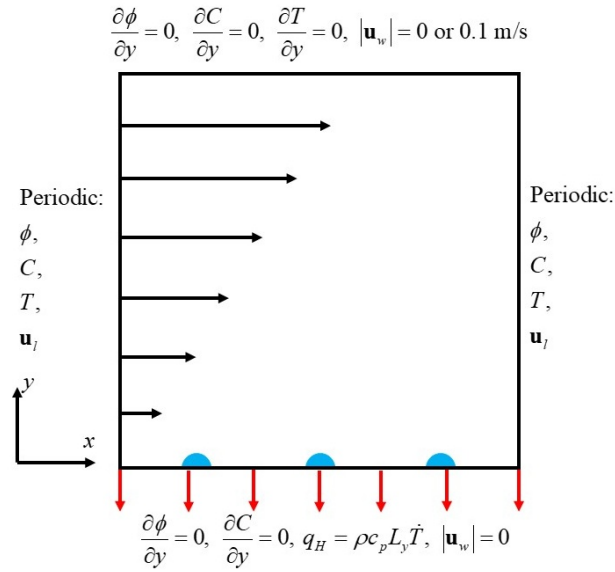


Fig. 2. Setup of boundary conditions.

### 3.1 Dendrite growth without latent heat

For comparison, dendrite growth is first simulated without the release of latent heat. Fig. 3 shows the simulation results. The grain identification (ID) 0 represents the liquid phase, while

other grain IDs represent solid phases with different orientations. Using the temperature gradient  $G = |\nabla T|$  and growth rate  $V$ , a solidification map is constructed based on the values of the local cooling rate  $GV$  and the ratio  $G/V$  [48]. The solidified microstructure can be equiaxed dendritic, columnar dendritic, cellular or planar as the ratio  $G/V$  increases. When the ratio  $G/V$  is small at the beginning of the simulation, the columnar dendritic growth pattern can be easily recognized at the time of 0.35 ms, as shown in Fig. 3(a). The primary arms and secondary arms can be differentiated without much difficulty. It is easy to observe that the primary arms of the dendrite grow faster than the secondary arms, as a result of the anisotropy of the interface energy. Without the release of latent heat, the secondary arms grow so fast that they quickly merge with each other as shown in Fig. 3(b-d). It is also seen in Fig. 3(d) that growth competition between grains of different orientations exists. Vertices or corners occur during dendrite growth, as highlighted by circles. The segregation of solute occurs at the solid-liquid interface because the solid phase has a lower composition than the liquid phase. High segregation of solute can be observed at the grain boundaries between secondary arms inside the grains, as shown in Fig. 3(e).

In this model, the effect of latent heat is not considered. As a result, the temperature is reduced monotonically from the top to the bottom of the simulation domain. At the same time, the detailed morphology of secondary arms cannot be observed, and there is no gap between grains. With the limitation of in-situ experimental methods, there is still no direct observation of dendrite growth under rapid solidification. For a slow solidification process, in-situ X-ray microscopy experiments [49] showed a much slower growth of secondary arms and that gaps between grains sustain for a long period during dendrite growth. Therefore, it is reasonable to suspect that the simulation without latent heat overestimates the solidification speed.

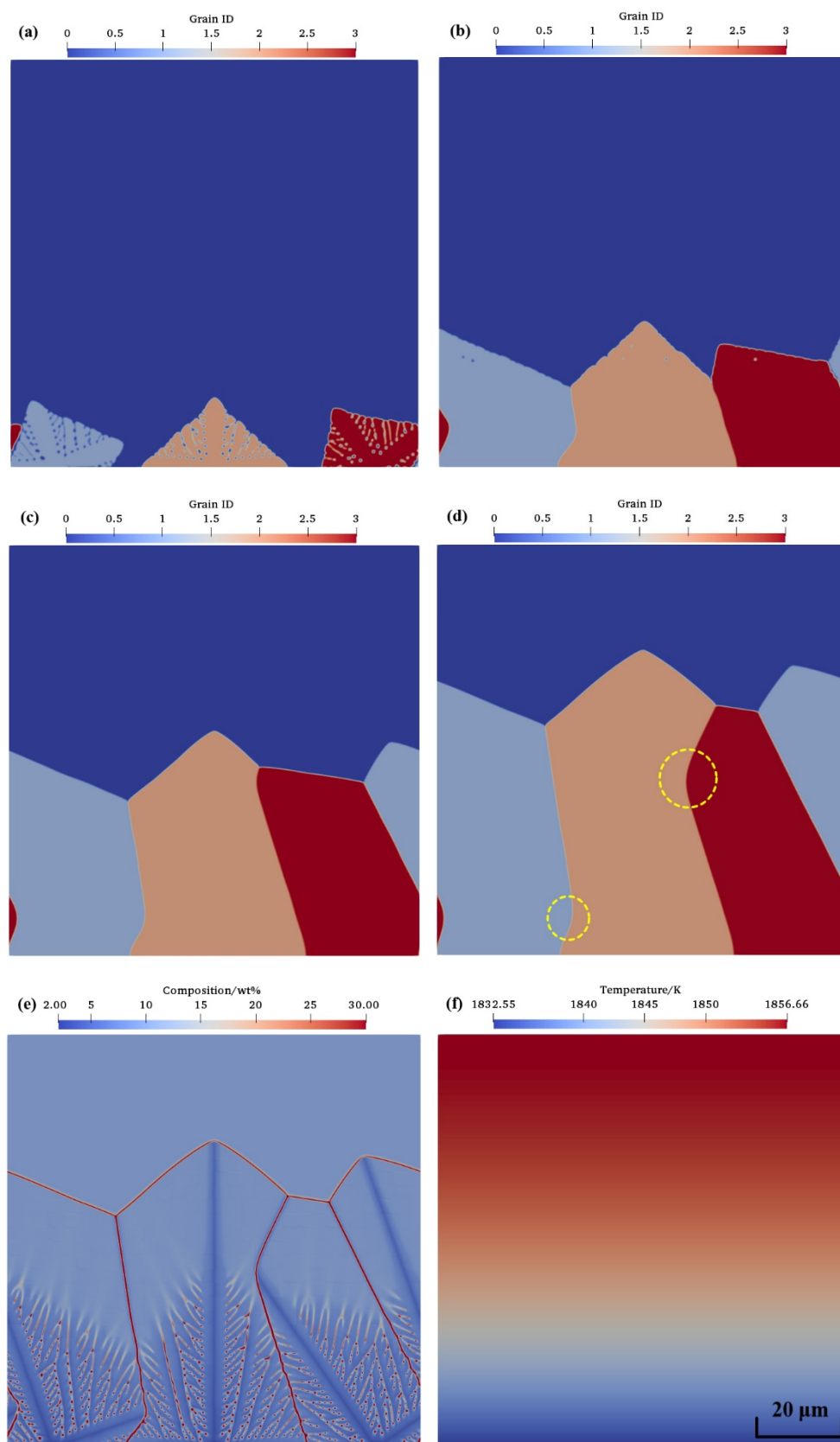


Fig. 3. Dendrite growth without latent heat. Phase field at (a) 0.35 ms, (b) 0.7 ms, (c) 1.05 ms, (d) 1.4 ms, (e) composition field at 1.4 ms, and (f) temperature field at 1.4 ms.

### ***3.2 Non-isothermal dendrite growth with latent heat***

In the second model, non-isothermal dendrite growth with the release of latent heat during the phase transition is considered. Fig. 4 shows the simulation results. The temperature field, composition distribution, and the morphology of the dendrite are quite different from the case of dendrite growth without latent heat in Section 3.1. The columnar dendritic growth pattern is shown in Fig. 4(a-d). Because of the release of latent heat, the temperature gradient  $G$  is smaller than that in the case without latent heat, which results in a lower ratio  $G/V$ . At the initial stage of growth, the columnar dendrites grow with the four-fold symmetry that is similar to equiaxed dendrites. Because of the high temperature gradient along the vertical direction, the vertical secondary arms become dominant, while the growth of horizontal secondary arms is suppressed. In Fig. 4(e), high segregation of solute can be observed at the grain boundaries and between secondary arms inside the grains, where some small portions of liquid are trapped and surrounded by the solid phase. The composition of trapped liquid phase increases as the liquid phase shrinks. The small pocket of liquid phase may remain liquid for a long period until solid diffusion takes away the remaining solute supersaturation before it is completely solidified. The degree of solute segregation at the solid-liquid phase decreases from the bottom to the top of the grains.

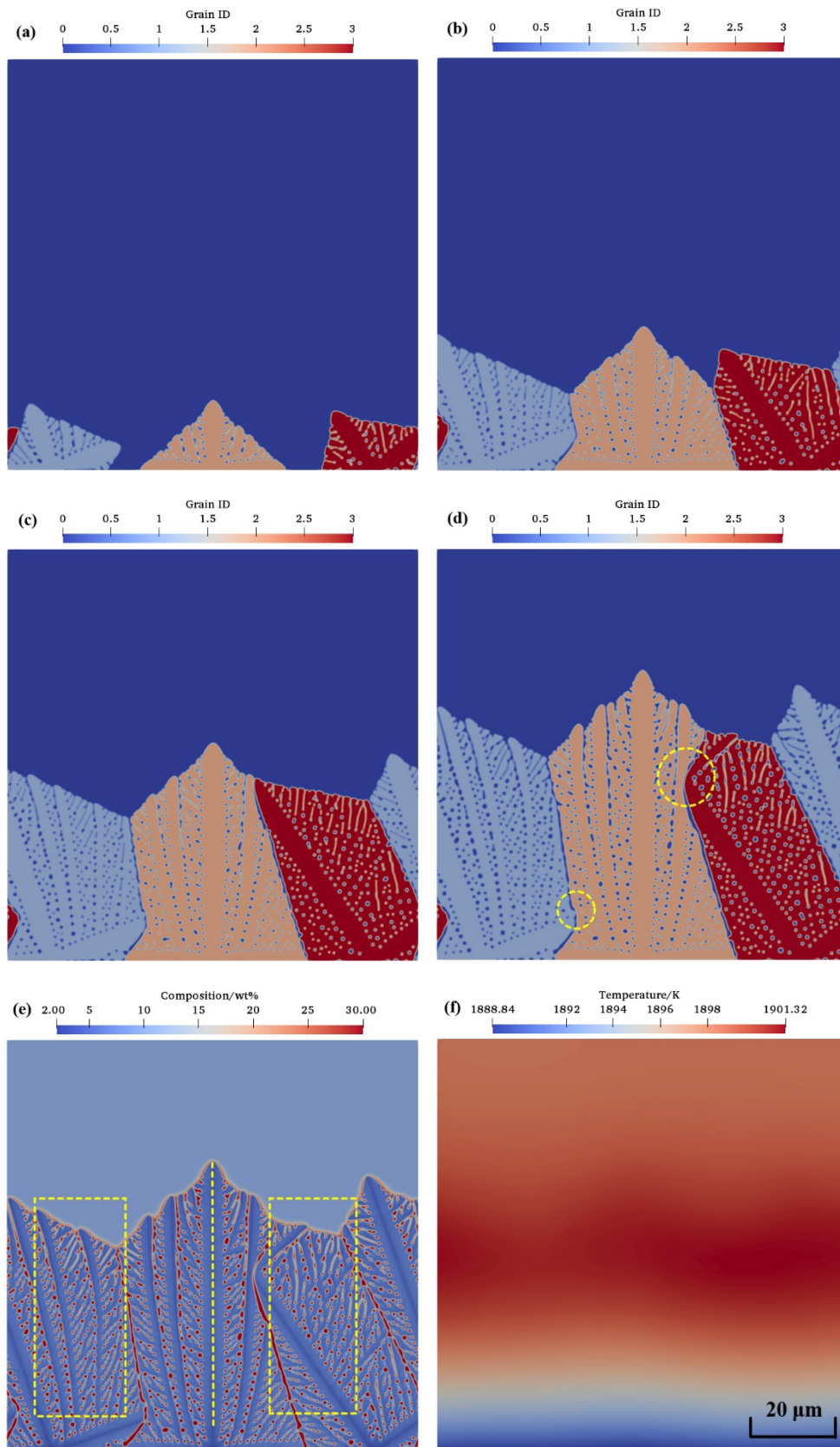


Fig. 4. Non-isothermal dendrite growth with latent heat. Phase field at (a) 0.35 ms, (b) 0.7 ms, (c) 1.05 ms, (d) 1.4 ms, (e) composition field at 1.4 ms, and (f) temperature field at 1.4 ms.

The simulated solute trapping is verified as follows. Based on the simulation results, the partition coefficient at the tips of dendrites is estimated as

$$k = \frac{C_s}{C_l} = \frac{3.96}{17.7} \approx 0.223 .$$

With  $V = 0.043$  m/s and  $D_l = 7.9 \times 10^{-9}$  m<sup>2</sup>/s, the partition coefficient, according to Aziz's model, is calculated as

$$k = \frac{k_e + V\lambda / D_l}{1 + V\lambda / D_l} \approx 0.219 ,$$

which is close to the above simulation result. The average temperature in the whole simulation domain is higher than that in the case without latent heat. The temperature of the solid phase is higher than that of the liquid phase, as shown in Fig. 4(f), which decreases the undercooling and the driving force of growth. The release of latent heat prevents the secondary arms from merging with each other quickly, which explains the columnar dendritic growth to some extent.

The simulation results suggest that it is important to consider heat transfer, especially latent heat, during the solidification process, which provides detailed composition, temperature, and grain growth pattern information.

### ***3.3 Non-isothermal dendrite growth with latent heat in a forced flow***

A further refinement of the model is to incorporate fluid flow. A constant flow velocity  $|\mathbf{u}_w| = 0.1$  m/s is imposed at the top boundary of the domain along the positive  $x$ -direction. Simulation results are shown in Fig. 5. Note that the magnitude of the velocity field is represented by the colors of the arrows rather than their sizes. The velocities corresponding to the arrows appearing in the solid phase region are near zero.

It is observed that the columnar dendrite morphology is slightly different from that in non-isothermal dendrite growth without flow. Compared to Fig. 4(e), the growth of some horizontal secondary arms in Fig. 5(e) is enhanced under the effect of flow, which is shown in the regions

highlighted with rectangles. In addition, the primary dendrite is inclined slightly under the forced flow, as the vertical dashed line in Fig. 5(e) indicates. When the flow encounters the continually growing dendrites, the local velocity field is disturbed. Some vortexes are observed in Fig. 5(a). The flow changes the dendrite morphology by affecting both the composition and the temperature field. The flow can accelerate grain growth by enhancing solute diffusion and increasing undercooling, which results in a higher driving force. It is also observed in Fig. 5(f) that the temperature and temperature gradient rise slightly in a forced flow. This is because the flow enhances the growth of some horizontal secondary arms and increases the release of latent heat. The simulation results suggest that the melt flow has some effect on dendrite growth. However, our sensitivity study shows that the rapid solidification can suppress the flow effect if velocity is relatively small.

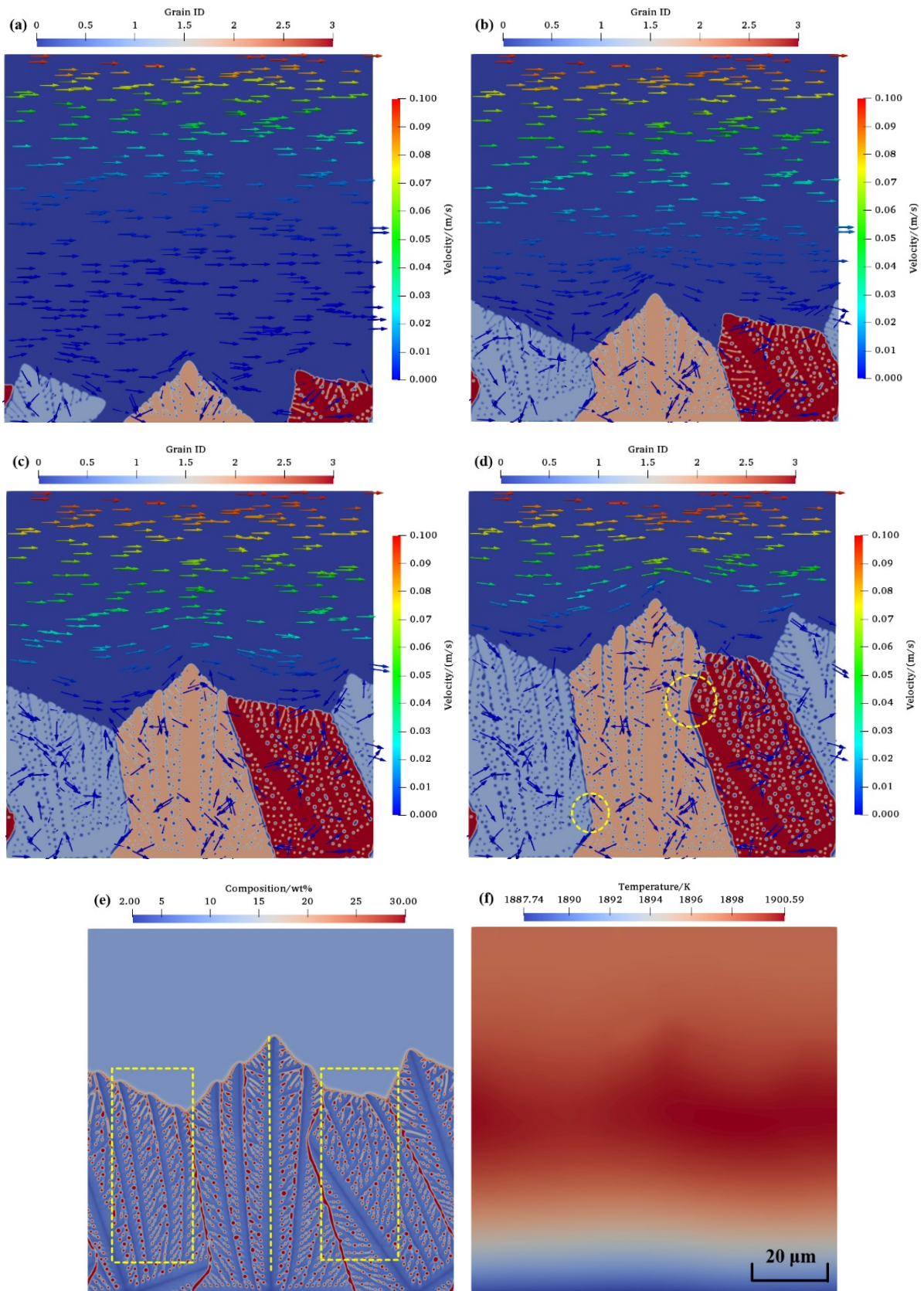


Fig. 5. Non-isothermal dendrite growth with latent heat in a forced flow. Phase field and flow field at (a) 0.35 ms, (b) 0.7 ms, (c) 1.05 ms, (d) 1.4 ms, (e) composition field at 1.4 ms, and (f) temperature field at 1.4 ms.

### 3.4 Experimental comparison

Solidification of Ti-6Al-4V has several pathways, including suppression of the reaction and primary beta phase formation, monovariant reactions, and invariant reactions for the residue alloy melt [51]. Our model simulates the rapid solidification process of Ti-6Al-4V with emphasis on primary beta phase formation. During the SLM process of Ti-6Al-4V alloy, the  $\beta$  phase is formed from the liquid. Then the prior  $\beta$  phase transforms to the acicular  $\alpha'$  martensite phase. This solid-state phase transition is described by the Burgers orientation relationship. However, the solid-state phase transition is not considered in our solidification simulation. Given that in-situ experimental observation of dendrite evolution during rapid solidification process is challenging, it is difficult to compare simulated dendrite morphology and growth with experimental observation directly.

Nevertheless, EBSD images of acicular  $\alpha'$  martensite phases, which originate from the parent  $\beta$  grains, are available. Here, the simulated dendrite morphology is compared with the reconstructed prior  $\beta$  phase orientation map from an EBSD image [47], as shown in Fig. 6. It is observed that acicular  $\alpha'$  martensite phases are formed in the prior columnar  $\beta$  grains. Usually, prior columnar  $\beta$  grains have a high aspect ratio because of the high temperature gradient along the building direction. The simulated dendrite morphology in Fig. 5(d) matches qualitatively with the prior columnar  $\beta$  grains, such as the bottom-right corner with a size of  $90 \times 90 \mu\text{m}$  in Fig. 6. The primary arm spacing is  $35 \mu\text{m}$ . Because of the growth competition between grains of different orientations, curved grain boundaries, highlighted by circles, are observed when two dendrites encounter each other, which was also predicted by simulations. Furthermore, the secondary arm spacing of the simulated microstructure is  $\lambda_2 = 1.2 \mu\text{m}$ , which is close to the calculated value  $\lambda_2 = 1.5 \mu\text{m}$  based on an analytical model proposed by Bouchard and Kirkaldy [50], as

$$\lambda_2 = 12\pi \left[ \frac{4\sigma}{C_0(1-k)^2 \rho L_H} \left( \frac{D_l}{V} \right)^2 \right]^{\frac{1}{3}}. \quad (33)$$

The difference between the predicted and observed secondary arm spacing is possibly caused by parameter uncertainty and model-form uncertainty. The parameter uncertainty can be

associated with the interface energy  $\sigma$ , latent heat  $L_H$ , solute diffusivity  $D_l$ , and local velocity of the interface  $V$ .

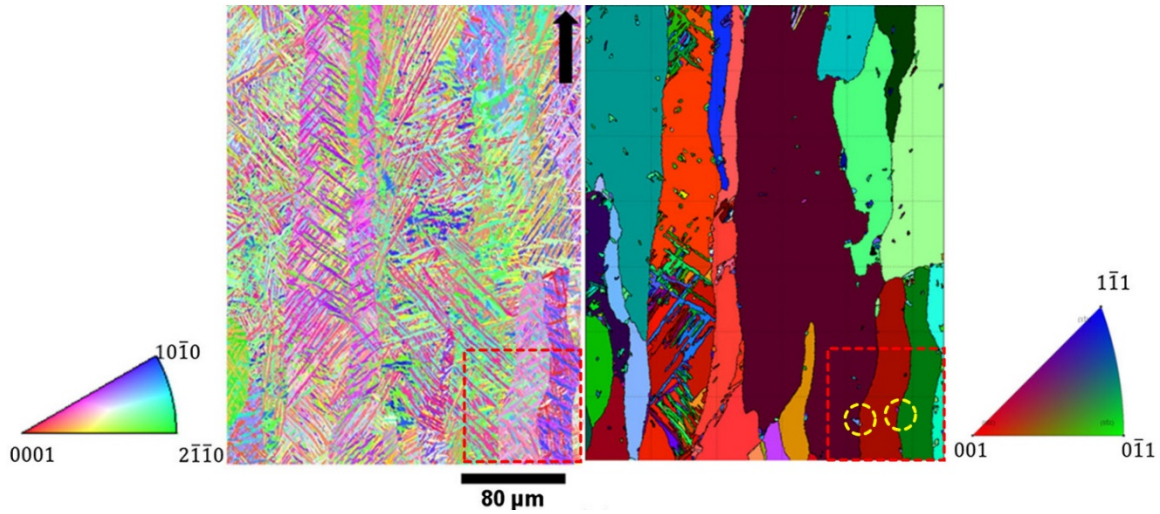


Fig. 6.  $\alpha'$  and corresponding reconstructed  $\beta$  orientation maps from EBSD data. Courtesy of Simonelli et al. [47]

### 3.5 Convergence study with finer mesh

To assess the sensitivity of mesh size on the simulation results, a finer mesh  $dx = 0.03 \mu\text{m}$  is used in the convergence study. Other simulation setups are kept the same. Fig. 7 shows the simulation results of dendrite growth without latent heat and non-isothermal dendrite growth with latent heat in a forced flow at 0.7 ms. After the mesh refinement, the difference in dendrite growth speed with and without latent heat becomes more obvious. Without latent heat, as shown in Fig. 7(a), some detailed morphology of secondary arms can now be observed around the dendrite tips, but not at the bottom of dendrites. In contrast, with latent heat, as shown in Fig. 7(c), the morphology has clear patterns of secondary arms that are similar to the ones in Fig. 5(b). The growth speed of dendrites using the fine mesh  $dx = 0.03 \mu\text{m}$  is almost the same as that in the coarse mesh  $dx = 0.1 \mu\text{m}$ . The dendrite growth slows down when latent heat is considered. The solute distribution with the fine mesh is also similar to that of the coarse mesh. The results further confirm that considering latent heat is necessary to reveal the details of secondary arms and provide more realistic kinetics of dendrite growth. Compared to the fine mesh, the simulation with the coarse mesh  $dx = 0.1 \mu\text{m}$  reveals enough details of dendrite growth and reduces the computational cost.

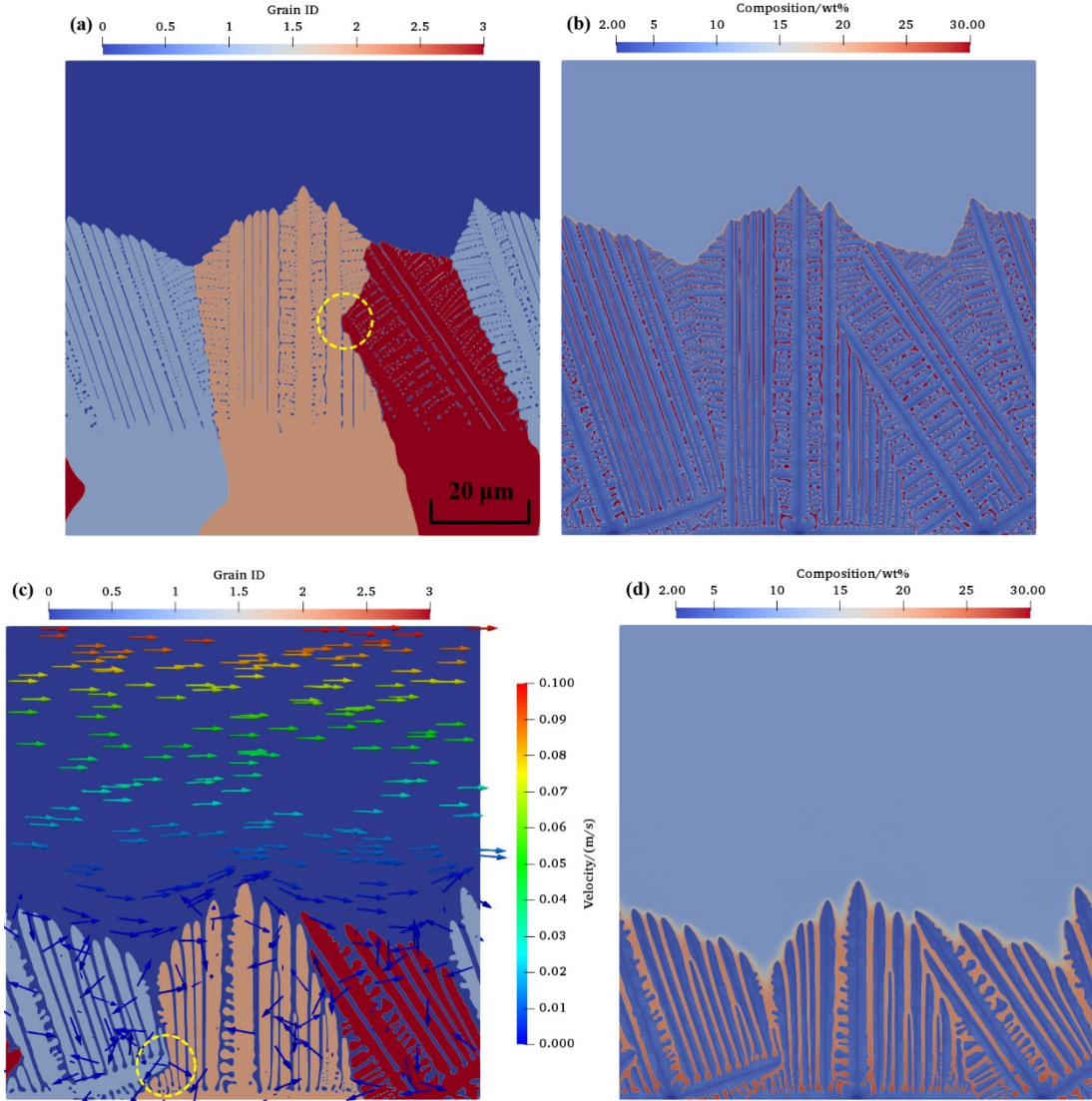


Fig. 7. With fine mesh, (a) phase field and (b) composition field in dendrite growth without latent heat at 0.7 ms; (c) phase field and flow field, and (d) composition field in non-isothermal dendrite growth with latent heat in a forced flow at 0.7 ms.

### 3.6 Quantitative analysis

To compare the effects on temperature quantitatively, the thermal histories in different simulation scenarios are plotted in Fig. 8, where the three curves are the temperatures observed at the location of  $x = 45 \mu\text{m}$  and  $y = 0 \mu\text{m}$  for the cases without latent heat, with latent heat, and with latent heat and flow, respectively. There is little difference in the thermal histories with and without considering melt flow, whereas considering latent heat gives a significantly different prediction. At the beginning of solidification ( $0 \leq t < 175 \mu\text{s}$ ), the effect of latent heat is not obvious because the fraction of phase transition is small. The temperature drops at a similar rate for all three cases. When  $t \geq 175 \mu\text{s}$ , the temperature without latent heat decreases

linearly. In contrast, the temperature with latent heat decreases slowly and starts to increase at  $t = 875 \mu\text{s}$  because of the continuous release of latent heat. The phenomenon is commonly known as recalescence during solidification of metals, similarly observed in the simulation results of Ref. [10].

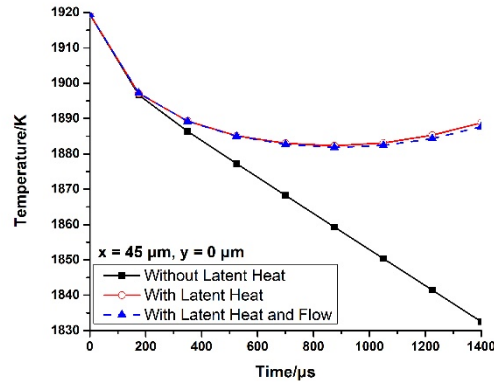


Fig. 8. Thermal histories at the location of  $x = 45 \mu\text{m}$ ,  $y = 0 \mu\text{m}$  under different conditions.

Fig. 9 shows the temperature distribution of non-isothermal dendrite growth along the  $y$ -direction at  $x = 45 \mu\text{m}$ . It is observed that the forced flow reduces the temperature values but increases the temperature gradients only slightly.

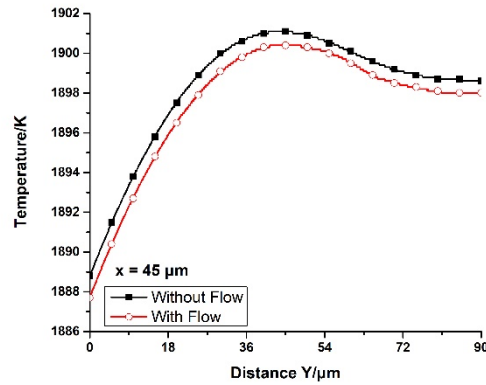


Fig. 9. The temperature distribution of non-isothermal dendrite growth along the vertical line at  $x = 45 \mu\text{m}$ .

Table 2 summarizes the dendrite tip temperature gradient  $G$ , dendrite tip growth velocity  $V$ , and their combinations for the three cases of simulations. When the release of latent heat is considered, the dendrite tip temperature gradient  $G$ , dendrite tip growth velocity  $V$ , and average growth velocity  $V_{ave}$  are smaller than those without latent heat. The local cooling rate  $GV$  and

the ratio  $G/V$  are also lower. When a forced flow is imposed, the dendrite tip temperature gradient  $G$  and dendrite tip growth velocity  $V$  slightly increase. This suggests that the forced flow can accelerate dendrite growth, resulting in further release of latent heat and a higher temperature gradient. The average growth velocities  $V_{ave}$  with the flow and without the flow are almost the same, which means that the release of latent heat can stabilize the dendrite growth. The local cooling rate  $GV$  and the ratio  $G/V$  increase slightly with the forced flow. The effect of melt flow on dendrite growth is suppressed by the rapid solidification.

Table 2. Quantitative analysis of simulation results

	Without latent heat	With latent heat	With latent heat and flow
Dendrite tip temperature gradient $G$ at 1.4 ms [K/mm]	130	80	100
Dendrite tip growth velocity $V$ at 1.4 ms [mm/s]	49	43	44
Average growth velocity $V_{ave}$ [mm/s]	46.9	44.7	45
Local cooling rate $GV$ [K/s]	6370	3440	4400
Ratio $G/V$ [K · s/mm <sup>2</sup> ]	2.65	1.86	2.27

#### 4. Conclusions

In this work, a mesoscale multi-physics model is developed to simulate the rapid solidification of Ti-6Al-4V alloy by integrating the phase-field method and the thermal lattice Boltzmann method. This model simulates the rapid solidification process of Ti-6Al-4V with emphasis on primary  $\beta$  phase formation. The model concurrently predicts solute transport, phase transition, heat transfer, latent heat, and melt flow. The local non-equilibrium partition coefficient is calculated based on Aziz's model to compute the solute distribution during rapid solidification. The diffusivity of the liquid is temperature-dependent, while other physical properties of Ti-6Al-4V are assumed to be constant. By considering the release of latent heat, the model can predict the composition distribution, temperature field, grain growth, and dendrite morphology with more detail than models without latent heat. The results show that considering latent heat is important for modeling thermal effects on the dendrite growth. The average growth rate  $V_{ave}$  is lower with latent heat than without it. The local cooling rate  $GV$  and the ratio  $G/V$  are lower as well. The recalescence occurs during the non-isothermal dendrite

growth.

The effect of fluid flow on dendrite growth is small under rapid solidification. The advection changes the distributions of temperature and composition. The flow can accelerate the grain growth by enhancing solute diffusion and increasing undercooling, which results in a higher driving force. The forced flow enhances the growth of horizontal secondary arms and increases the temperature gradient slightly.

The simultaneous considerations of solute transport, kinetics of phase transition, and thermal effects are necessary to understand rapid solidification. The multi-physics modeling approach can elucidate the complex physical processes with more details. The challenge of coupling multiple physical effects is the highly varied time scales used in these simulated processes. Because of the high cooling rate in rapid solidification, the time step needs to be small enough for numerical stability. However, the dimensionless relaxation time in TLBM should be greater than 0.5 and not much larger than 1 because of truncation errors [52]. The trade-offs mostly rely on sensitivity studies. In our model, a variable grid approach is taken to treat PFM and TLBM separately to alleviate this problem.

There are several approximations in our model that may affect the accuracy of predictions. First, the interface mobility is assumed to be constant. However it depends on temperature in reality. Since there is a lack of experimental results, molecular dynamics simulations can be applied to estimate mobility and assess the influential factors such as temperature. Interatomic potentials for Ti-6Al-4V alloy for molecular dynamics nevertheless need to be developed. Second, the pseudo-binary approach is adopted to model the ternary alloy. However, Al and V will not be trapped in the same way during rapid solidification. A multi-component multi-phase model is needed to reveal further details. Third, to simulate the complete process of SLM, nucleation and solid-state phase transition should also be considered to predict the final microstructure. This allows for direct quantitative comparison and model validation based on existing experimental capabilities. Some emerging in-situ characterization techniques for rapid solidification such as dynamic transmission electron microscopy [53] can help calibrate and validate models. Fourth, the current model is only applied to the 2D domain. Future work will

include the extension to 3D domains. 3D models will be much more computationally demanding. Parallelization is a viable solution to this issue. Both the phase-field method and the thermal lattice Boltzmann method can be easily adapted for parallel computation.

## References

- [1] S.G. Kim, W.T. Kim, T. Suzuki, Phase-field model for binary alloys., *Phys. Rev. E. Stat. Phys. Plasmas. Fluids. Relat. Interdiscip. Topics.* 60 (1999) 7186–7197. doi:10.1103/PhysRevE.60.7186.
- [2] W.J. Boettinger, J. A. Warren, Simulation of the cell to plane front transition during directional solidification at high velocity, *J. Cryst. Growth.* 200 (1999) 583–591. doi:10.1016/S0022-0248(98)01063-X.
- [3] L.-Q. Chen, Phase -Field Models for Microstructure Evolution, *Annu. Rev. Mater. Res.* 32 (2002) 113–140. doi:10.1146/annurev.matsci.32.112001.132041.
- [4] I. Singer-Loginova, H.M. Singer, The phase field technique for modeling multiphase materials, *Reports Prog. Phys.* 71 (2008) 106501. doi:10.1088/0034-4885/71/10/106501.
- [5] N. Moelans, B. Blanpain, P. Wollants, An introduction to phase-field modeling of microstructure evolution, *Calphad Comput. Coupling Phase Diagrams Thermochem.* 32 (2008) 268–294. doi:10.1016/j.calphad.2007.11.003.
- [6] I. Steinbach, Phase-field models in materials science, *Model. Simul. Mater. Sci. Eng.* 17 (2009) 73001. doi:10.1088/0965-0393/17/7/073001.
- [7] I. Steinbach, Why solidification? Why phase-field?, *Jom.* 65 (2013) 1096–1102. doi:10.1007/s11837-013-0681-5.

- [8] A. Choudhury, K. Reuther, E. Wesner, A. August, B. Nestler, M. Rettenmayr, Comparison of phase-field and cellular automaton models for dendritic solidification in Al-Cu alloy, *Comput. Mater. Sci.* 55 (2012) 263–268. doi:10.1016/j.commatsci.2011.12.019.
- [9] C. Beckermann, H.-J. Diepers, I. Steinbach, a Karma, X. Tong, Modeling Melt Convection in Phase-Field Simulations of Solidification, *J. Comput. Phys.* 154 (1999) 468–496. doi:10.1006/jcph.1999.6323.
- [10] I. Loginova, G. Amberg, J. Ågren, Phase-field simulations of non-isothermal binary alloy solidification, *Acta Mater.* 49 (2001) 573–581. doi:10.1016/S1359-6454(00)00360-8.
- [11] C.W. Lan, C.J. Shih, Phase field simulation of non-isothermal free dendritic growth of a binary alloy in a forced flow, *J. Cryst. Growth.* 264 (2004) 472–482. doi:10.1016/j.jcrysgro.2004.01.016.
- [12] J.C. Ramirez, C. Beckermann, a Karma, H.-J. Diepers, Phase-field modeling of binary alloy solidification with coupled heat and solute diffusion., *Phys. Rev. E. Stat. Nonlin. Soft Matter Phys.* 69 (2004) 51607. doi:10.1103/PhysRevE.69.051607.
- [13] B. Nestler, H. Garcke, B. Stinner, Multicomponent alloy solidification: Phase-field modeling and simulations, *Phys. Rev. E - Stat. Nonlinear, Soft Matter Phys.* 71 (2005) 1–6. doi:10.1103/PhysRevE.71.041609.
- [14] I. Steinbach, M. Apel, Multi phase field model for solid state transformation with elastic strain, *Phys. D Nonlinear Phenom.* 217 (2006) 153–160. doi:10.1016/j.physd.2006.04.001.
- [15] X. Gong, K. Chou, Phase-field modeling of microstructure evolution in electron beam additive manufacturing, *Jom.* 67 (2015) 1176–1182. doi:10.1007/s11837-015-1352-5.
- [16] S. Sahoo, K. Chou, Phase-field simulation of microstructure evolution of Ti-6Al-4V in electron beam additive manufacturing process, *Addit. Manuf.* 9 (2016) 14–24. doi:10.1016/j.addma.2015.12.005.

- [17] C.K. Aidun, J.R. Clausen, G.W. Woodruff, Lattice-Boltzmann Method for Complex Flows, *Annu. Rev. Fluid Mech.* 42 (2010) 439–72. doi:10.1146/annurev-fluid-121108-145519.
- [18] S. Chen, G.D. Doolen, Lattice Boltzmann Method for Fluid Flows, *Annu. Rev. Fluid Mech.* 84 (1998) 16704. doi:10.1146/annurev.fluid.30.1.329.
- [19] Q. Li, K.H. Luo, Q.J. Kang, Y.L. He, Q. Chen, Q. Liu, Lattice Boltzmann methods for multiphase flow and phase-change heat transfer, *Prog. Energy Combust. Sci.* 52 (2016) 62–105. doi:10.1016/j.pecs.2015.10.001.
- [20] X. He, S. Chen, G.D. Doolen, A novel thermal model for the lattice Boltzmann method in incompressible limit, *J. Comput. Phys.* 146 (1998) 282–300.
- [21] S. Chakraborty, D. Chatterjee, An enthalpy-based hybrid lattice-Boltzmann method for modelling solid–liquid phase transition in the presence of convective transport, *J. Fluid Mech.* 592 (2007) 155–175. doi:10.1017/S0022112007008555.
- [22] Z. Guo, C. Zheng, B. Shi, T.S. Zhao, Thermal lattice Boltzmann equation for low Mach number flows: Decoupling model, *Phys. Rev. E - Stat. Nonlinear, Soft Matter Phys.* 75 (2007) 1–15. doi:10.1103/PhysRevE.75.036704.
- [23] E. Attar, C. Körner, Lattice Boltzmann model for thermal free surface flows with liquid-solid phase transition, *Int. J. Heat Fluid Flow.* 32 (2011) 156–163. doi:10.1016/j.ijheatfluidflow.2010.09.006.
- [24] M. Eshraghi, S.D. Felicelli, An implicit lattice Boltzmann model for heat conduction with phase change, *Int. J. Heat Mass Transf.* 55 (2012) 2420–2428. doi:10.1016/j.ijheatmasstransfer.2012.01.018.
- [25] T. Seta, Implicit temperature-correction-based immersed-boundary thermal lattice Boltzmann method for the simulation of natural convection, *Phys. Rev. E - Stat. Nonlinear, Soft Matter Phys.* 87 (2013) 1–16.

- doi:10.1103/PhysRevE.87.063304.
- [26] D.A. Perumal, A.K. Dass, A Review on the development of lattice Boltzmann computation of macro fluid flows and heat transfer, *Alexandria Eng. J.* 54 (2015) 955–971. doi:10.1016/j.aej.2015.07.015.
- [27] R. Ammer, M. Markl, U. Ljungblad, C. Körner, U. Rüde, Simulating fast electron beam melting with a parallel thermal free surface lattice Boltzmann method, *Comput. Math. with Appl.* 67 (2014) 318–330. doi:10.1016/j.camwa.2013.10.001.
- [28] D. Medvedev, K. Kassner, Lattice Boltzmann scheme for crystal growth in external flows, *Phys. Rev. E - Stat. Nonlinear, Soft Matter Phys.* 72 (2005) 1–10. doi:10.1103/PhysRevE.72.056703.
- [29] W. Miller, I. Rasin, S. Succi, Lattice Boltzmann phase-field modelling of binary-alloy solidification, *Phys. A Stat. Mech. Its Appl.* 362 (2006) 78–83. doi:10.1016/j.physa.2005.09.021.
- [30] D. Medvedev, F. Varnik, I. Steinbach, Simulating mobile dendrites in a flow, *Procedia Comput. Sci.* 18 (2013) 2512–2520. doi:10.1016/j.procs.2013.05.431.
- [31] R. Rojas, T. Takaki, M. Ohno, A phase-field-lattice Boltzmann method for modeling motion and growth of a dendrite for binary alloy solidification in the presence of melt convection, *J. Comput. Phys.* 298 (2015) 29–40. doi:10.1016/j.jcp.2015.05.045.
- [32] T. Takaki, R. Rojas, M. Ohno, T. Shimokawabe, T. Aoki, GPU phase-field lattice Boltzmann simulations of growth and motion of a binary alloy dendrite, *IOP Conf. Ser. Mater. Sci. Eng.* 84 (2015) 12066. doi:10.1088/1757-899X/84/1/012066.
- [33] S. Sakane, T. Takaki, R. Rojas, M. Ohno, Y. Shibuta, T. Shimokawabe, T. Aoki, Multi-GPUs parallel computation of dendrite growth in forced convection using the phase-field-lattice Boltzmann model, *J. Cryst. Growth.* (2016) 1–6. doi:10.1016/j.jcrysgro.2016.11.103.

- [34] G.J. Schmitz, B. Böttger, M. Apel, On the role of solidification modelling in Integrated Computational Materials Engineering “ICME,” IOP Conf. Ser. Mater. Sci. Eng. 117 (2016) 12041. doi:10.1088/1757-899X/117/1/012041.
- [35] D. Liu, Y. Wang, Mesoscale multi-physics simulation of solidification in selective laser melting process using a phase field and thermal lattice Boltzmann model, in: 2017 ASME Int. Des. Eng. Tech. Conf. Comput. Inf. Eng. Conf., Cleveland, Ohio, Aug.6-9, 2017: p. Paper No.DETC2017-67633.
- [36] M.J. Aziz, Model for solute redistribution during rapid solidification, J. Appl. Phys. 53 (1982) 1158–1168. doi:10.1063/1.329867.
- [37] N.A. Ahmad, A.A. Wheeler, W.J. Boettinger, G.B. McFadden, Solute trapping and solute drag in a phase-field model of rapid solidification, Phys. Rev. E. 58 (1998) 3436–3450. doi:10.1103/PhysRevE.58.3436.
- [38] S.L. Semiatin, V.G. Ivanchenko, O.M. Ivasishin, Diffusion models for evaporation losses during electron-beam melting of alpha/beta-titanium alloys, Metall. Mater. Trans. B. 35 (2004) 235–245. doi:10.1007/s11663-004-0025-5.
- [39] S.G. Kim, A phase-field model with antitrapping current for multicomponent alloys with arbitrary thermodynamic properties, Acta Mater. 55 (2007) 4391–4399. doi:10.1016/j.actamat.2007.04.004.
- [40] Z. Guo, C. Zheng, B. Shi, Discrete lattice effects on the forcing term in the lattice Boltzmann method, Phys. Rev. E - Stat. Nonlinear, Soft Matter Phys. 65 (2002) 1–6. doi:10.1103/PhysRevE.65.046308.
- [41] I. Ginzburg, Generic boundary conditions for lattice Boltzmann models and their application to advection and anisotropic dispersion equations, Adv. Water Resour. 28 (2005) 1196–1216. doi:10.1016/j.advwatres.2005.03.009.
- [42] T. Zhang, B. Shi, Z. Guo, Z. Chai, J. Lu, General bounce-back scheme for concentration boundary

- condition in the lattice-Boltzmann method, *Phys. Rev. E - Stat. Nonlinear, Soft Matter Phys.* 85 (2012) 1–14. doi:10.1103/PhysRevE.85.016701.
- [43] Q. Chen, X. Zhang, J. Zhang, Improved treatments for general boundary conditions in the lattice Boltzmann method for convection-diffusion and heat transfer processes, *Phys. Rev. E.* 88 (2013) 33304. doi:10.1103/PhysRevE.88.033304.
- [44] OpenPhase, (2017). <http://www.openphase.de/>.
- [45] L. Nastac, Solute Redistribution, Liquid/Solid Interface Instability, and Initial Transient Regions during the Unidirectional Solidification of Ti-6-4 and Ti-17 Alloys, in: *CFD Model. Simul. Mater. Process.*, Wiley-TMS, New York, 2012: pp. 123–130.
- [46] H. Helmer, A. Bauereiß, R.F. Singer, C. Körner, Grain structure evolution in Inconel 718 during selective electron beam melting, *Mater. Sci. Eng. A.* 668 (2016) 180–187. doi:10.1016/J.MSEA.2016.05.046.
- [47] M. Simonelli, Y.Y. Tse, C. Tuck, On the texture formation of selective laser melted Ti-6Al-4V, *Metall. Mater. Trans. A Phys. Metall. Mater. Sci.* 45 (2014) 2863–2872. doi:10.1007/s11661-014-2218-0.
- [48] S. Kou, *Welding Metallurgy*, 2nd ed., John Wiley & Sons, Hoboken, NJ, 2003.
- [49] L. Arnberg, R.H. Mathiesen, The real-time, high-resolution x-ray video microscopy of solidification in aluminum alloys, *JOM.* 59 (2007) 20–26. doi:10.1007/s11837-007-0099-z.
- [50] D. Bouchard, J.S. Kirkaldy, Equations and Specification of Predictive Procedures, *Metall. Mater. Trans. B.* 28B (1996) 651–663. <http://www.springerlink.com/index/763J07120X616164.pdf>.
- [51] S.L. Wei, L.J. Huang, J. Chang, S.J. Yang, Y.T. Ma, L. Geng, Containerless Rapid Solidification of Liquid Ti-Al-V Alloys Inside Drop Tube, *Proc. 13th World Conf. Titan.* (2016) 397–404. doi:10.1002/9781119296126.ch62.

- [52] D.J. Holdych, D.R. Noble, J.G. Georgiadis, R.O. Buckius, Truncation error analysis of lattice Boltzmann methods, *J. Comput. Phys.* 193 (2004) 595–619. doi:10.1016/j.jcp.2003.08.012.
- [53] J.-L.F. and J.T.M. Aurelien Perron, John D Roehling, Patrice E A Turchi, Matching time and spatial scales of rapid solidification: Dynamic TEM experiments coupled to CALPHAD-informed phase-field simulations, (2017) 0–15. doi:<https://doi.org/10.1088/1478-3975/aa9768>.